Solid State Electronics 168 (2020) 107726

Contents lists available at ScienceDirect

Solid State Electronics

journal homepage: www.elsevier.com/locate/sse

Electron-hole bilayer light-emitting device: Concept and operation

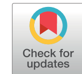

Gaurav Gupta, Florian Mema, Raymond J.E. Hueting (Senior Member, IEEE)*

MESA+ Institute, University of Twente, Enschede, The Netherlands

A R T I C L E I N F O

The review of this paper was arranged by "Joris Lacord"

Keywords:
Electrostatic doping
Light emission
Thermal generation
Ultra-thin body
III-V on-insulator

A B S T R A C T

We report a novel switched-mode light-emitting device (LED) in an undoped ultra-thin-body (UTB) based on the electrostatically-induced electron-hole bilayer (EHB) concept. The proposed device works on the principle of formation of EHB channels by applying suitable gate biases during the charging-cycle, and their recombination during a discharging-cycle. Using TCAD simulations, we show that continuous switching of the gates in an indium arsenide (InAs) based EHB LED with a ~12 μs time period leads to radiative recombination of the induced charge carriers with a peak internal quantum efficiency (IQE) as high as ~92% and a time-averaged IQE of ~29%. The proposed concept obviates the need for chemically doped p-n junctions in the UTB device for light-emitting applications. However, when relying on the thermal generation alone as a source of charge carriers in a small undoped semiconductor volume, a narrow bandgap semiconductor (such as InAs) is required for the proposed LED which ultimately limits the switching speed. For wider bandgap materials, highly doped regions on either side of the intrinsic UTB layer in the form of a lateral PIN structure could be employed where switching speed is then not limited by thermal generation. TCAD simulations of a silicon (Si) EHB LED based on such a gated PIN structure shows switching capability in the GHz frequency range making it attractive for SOI based optocoupling applications.

1. Introduction

Light-emitting devices based on ultra-thin-body (UTB) semiconductor-on-insulator technology are interesting candidates for inter-chip and intra-chip optical interconnect [1,2] as well as for sensing applications [3]. In addition to their attractiveness for integration with SOI technology, the UTB based light sources also benefit from their improved efficiency due to quantum confinement, and weak re-absorption of emitted photons inside their ultra-thin active region [4]. To realize such devices, a sharp junction in the UTB semiconductor is one essential requirement which is technologically challenging [5] in conventional chemical doping approaches. In this direction, electrostatic doping (ED) ([6] and references therein) has been widely explored as a potential alternative to chemical doping for UTB devices in Si and emerging semiconductors. Particularly, the electrostatically induced electron-hole bilayer (EHB) [7] is an interesting concept where charge carriers of opposite polarity are simultaneously induced in a dual gate UTB device. Such a concept has been extensively investigated for tunnel field effect transistors (TFETs) applications in various material systems and geometries [7–9]. A similar concept has also been reported for capacitor-less DRAM memory [10]. However, so far the EHB concept has not been reported for light emission via electroluminescence. In this work [11], we propose a novel light-emitting device (LED) based on the EHB concept in an undoped UTB channel.

2. Theory and device operation

The schematic cross-section of the proposed device is shown in Fig. 1. The proposed device is a dual gate structure with an UTB semiconductor as a channel material. It comprises two different (low-high) workfunction metals as top and bottom gate electrodes which are oppositely biased during the device operation. In the simulations the semiconductor body is kept floating. In practice the body can be grounded further away from the active gated device region via a side body contact as discussed in Section 3.2.

In the dual gate structure as shown in Fig. 1 with different top and bottom gate workfunctions and opposite biasing, electron and hole channels can be simultaneously induced [7]. To describe the workfunction and bias-induced charge carriers near each gate in such a fully-depleted UTB channel, the following equations (Eqs. 1,2) for the vertical electric field (E_s) and surface potential ($\psi_{sT,B}$) at both gate interfaces were derived before [6,12] assuming negligible charge carrier concentration:

* Corresponding author.
E-mail address: g.gupta@utwente.nl (G. Gupta).

https://doi.org/10.1016/j.sse.2019.107726

Available online 04 December 2019
0038-1101/ © 2020 The Authors. Published by Elsevier Ltd. This is an open access article under the CC BY license (http://creativecommons.org/licenses/BY/4.0/).

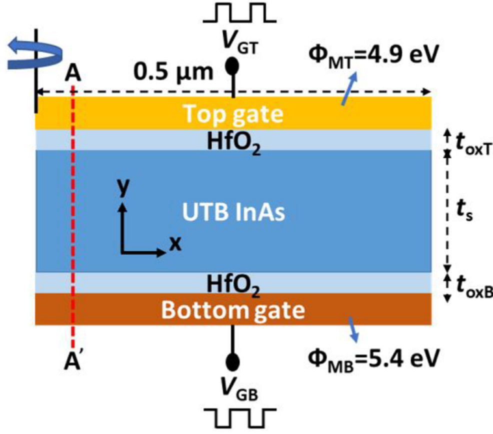

Fig. 1. Schematic cross-section of the proposed electron-hole bilayer InAs LED.

$$E_s = \frac{(V_{GT} - V_{GB}) - (\phi_{mT} - \phi_{mB})}{\frac{\varepsilon_s}{\varepsilon_{ox}}(t_{oxT} + t_{oxB}) + t_s}, \quad (1)$$

$$\psi_{sT,B} = V_{GT,B} \mp \frac{\varepsilon_s E_s}{C_{oxT,B}} - \Delta\phi_{mT,B}, \quad (2)$$

where the subscripts T and B refer to the top and bottom gate, respectively. $V_{GT,B}$ is the gate voltage, $\phi_{mT,B}$ is the gate metal workfunction, $\Delta\phi_{mT,B}$ is gate-body workfunction difference, $C_{oxT,B}$ is the areal oxide capacitance, t_{ox} and t_s are the oxide and semiconductor thickness, respectively, and ε_{ox} and ε_s are the oxide and semiconductor dielectric constant, respectively.

Eq. (1) expresses the field for the EHB formation in the coupled dual gate system. E_s also determines the field in the gate oxides, and as a result the maximum bias settings in the EHB device can be determined from this equation. Semi-classically, electrons will be induced near the top gate electrode if $\psi_{sT} > 0$ with a density at the interface $n = n_i \exp(\psi_{sT}/u_T)$ where n_i is the intrinsic concentration and u_T is the thermal voltage ($=kT/q$, where k is Boltzmann's constant, T is the temperature and q is the elementary charge). Similarly, if $\psi_{sB} < 0$ holes will be induced near the bottom gate electrode with a density at the interface $p = n_i \exp(-\psi_{sB}/u_T)$. However, since the influence of the mobile charge was neglected for the derivation of Eqs. (1) and (2), these are therefore not valid for a strong inversion situation. Moreover, quantum effects can modify the carrier densities and their distribution [13]. Further, the effect of interface trap charges can be accounted for as described in [6].

In the proposed EHB structure, which is similar to a parallel plate capacitor, the induced charge carriers remain fixed near their respective gate interfaces in steady state and do not recombine. However, the EHB device becomes electrically active as soon as (one or) both gates are switched between their charged- and discharged-state. During the discharging-cycle, the electron and hole distribution will gradually decay with time via recombination processes. Carrier recombination in a direct bandgap material has a high chance to be radiative. The result will be then light emission during a switching transient. Steady light output could therefore be obtained by continuously switching the gates.

InAs is an interesting material in this context because of its narrow and direct bandgap (E_g = 0.354 eV at 300 K) which first makes it more suitable for ED [6]. Second, the small E_g also results in a higher thermal generation rate of charge carriers which along with Shockley-Read-Hall (SRH) lifetime (τ_{SRH}) determines the switching speed in the proposed device. A simplified expression for time t_{th} required to thermally generate n_0 level of carriers from its intrinsic concentration n_i can be derived from the continuity equations as (see Appendix):

$$t_{th} = \frac{n_0}{\frac{n_i}{2 \cdot \tau_{SRH}} + B_{rad} \cdot n_i^2}, \quad (3)$$

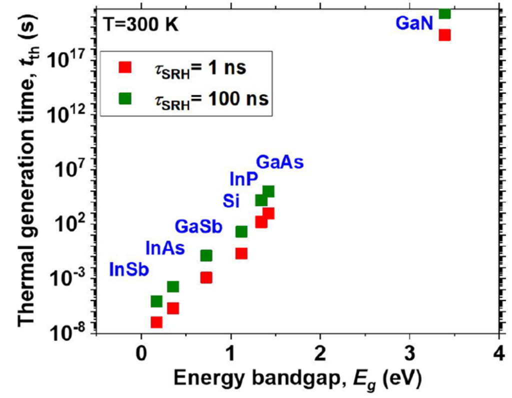

Fig. 2. Calculated carrier thermal generation time using Eq. (3) for various direct bandgap semiconductors (and Si) to reach a carrier concentration of ~10^{18} cm^{-3} from their intrinsic level shown for two different τ_{SRH}.

where B_{rad} is the radiative recombination coefficient.

Fig. 2 shows t_{th} against E_g, required to thermally generate $n_0 = 10^{18}$ cm^{-3} carriers for various direct bandgap semiconductors and Si, calculated using Eq. (3), from their respective intrinsic carrier level. For narrow bandgap semiconductors such as InAs (τ_{SRH} ~1 ns [14]), t_{th} is in a few µs range while for a wide bandgap material such as GaN, it is in order of 10^{17} s, indicating that the proposed device concept will only work for the former case.

Previously, both an electron [15] and a hole [16] inversion layer was observed in InAs MOS capacitors even at frequencies as high as 1 MHz suggesting a t_{th} in the µs range, which agrees well with Eq. (3). Further, an UTB InAs-on-insulator (XOI) technology suitable for realizing the proposed device has been experimentally demonstrated [17,18].

3. Results and discussion

3.1. Simulation parameters and models

The proposed device (Fig. 1) was investigated via 2-D TCAD simulations with cylindrical symmetry around y-axis using Sentaurus [19], applying Fermi-Dirac statistics with doping [20] and field dependent mobility models [21]. For recombination, standard SRH, Auger and radiative models [19] were included without taking into account any surface recombination at semiconductor-oxide interfaces. Also, the density gradient model [22,23] was used to account for quantum confinement effects. A low/high workfunction (ϕ_{mT} = 4.9 eV, ϕ_{mB} = 5.4 eV) was used for the top/bottom gate for inducing electrons/holes. The chosen gate metal workfunctions are reasonably symmetric with respect to the midgap workfunction (ϕ_{midgap} = 5.18 eV) of intrinsic InAs. The InAs body thickness (t_s) of 25 nm was chosen to balance the trade-off between the induced charge carrier concentration and their radiative recombination rate. Moreover the chosen thickness is well-outside the range of supercoupling effect [24,25], which otherwise becomes dominant at smaller thicknesses and prevent the co-existence of electron and hole channels. Hafnium dioxide (HfO_2) with $t_{oxT/oxB}$ = 4 nm was used for both gate dielectrics which provides a sufficiently high conduction band (ΔE_c) and valence band (ΔE_v) discontinuity as to prevent gate leakage (see Fig. 3(a)). Ideal interfaces without any traps or fixed charges were assumed. All simulations were performed at 300 K. Table 1 summarizes the parameter values used in this work.

3.2. Device operation: InAs EHB LED

In UTB devices, the electric field inside the semiconductor body is practically constant (see e.g. Fig. 3(a)). The electric field inside the InAs

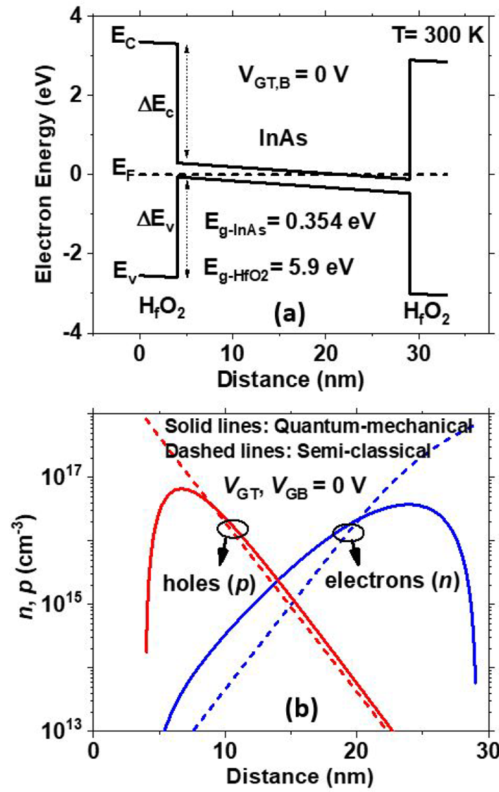

Fig. 3. TCAD simulations at thermal equilibrium, (a) energy band diagram taken along AA′ (see Fig. 1). (b) charge carrier profile taken along AA′.

Table 1
TCAD simulation parameters for InAs EHB LED at 300 K [19].

Parameter	Value
InAs bandgap, E_g, electron affinity, χ	0.354 eV, 5.06 eV
HfO_2 bandgap, E_g, electron affinity, χ	5.9 eV, 2.05 eV
Electron effective density of states mass, m_c	0.023 m_0
Hole effective density of states mass, m_v	0.48 m_0
Conduction band effective density of states, N_c	9.3×10^{16} cm^{-3}
Valence band effective density of states, N_v	8.4×10^{18} cm^{-3}
Radiative recombination coefficient, B_{rad}	1.1×10^{-10} cm^3 s^{-1}
SRH lifetime, τ_{SRH}	1 ns
Auger recombination coefficient	10^{-30} cm^6/s
Dielectric constant, ϵ_s, ϵ_{ox}	14ϵ_0, 22ϵ_0
Thickness, t_s, t_{ox}	25 nm, 4 nm
Gate Workfunction, ϕ_{mT}, ϕ_{mB}	4.9 eV, 5.4 eV

body decreases for a larger thickness and increases as the gate biases are raised to higher voltages as shown in Fig. 4. The calculated electric field (Eq. (1)) for weak inversion condition, i.e. either small body thicknesses or low gate voltages, is in good agreement with the TCAD simulation results. Some deviation between the model and TCAD is observed for strong inversion condition, *i.e.*, when large body thicknesses ($t_s \gtrsim 20$ nm) or high gate voltages ($|V_{GT,B}| \gtrsim 0.25$ V) are used. This can be explained by the influence of the high charge carrier concentration on the electrostatic potential which is not taken into account in Eq. (1).

The charge carrier profiles formed by workfunction induced ED at thermal equilibrium are shown in Fig. 3(b). The induced electron layer is relatively thick compared to the hole layer, as also observed experimentally [15], and is attributed to the relatively small electron effective (density of states) mass, m_c, which results in a small conduction band effective density of states, N_c. The carrier concentrations can be further increased by applying a small (~0.75 V) positive (negative) bias

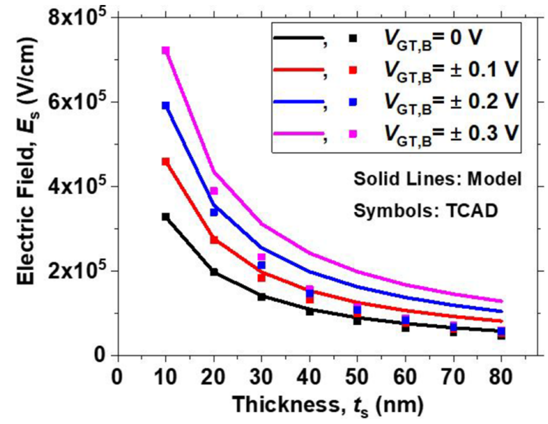

Fig. 4. Vertical electric field E_s in the InAs layer against the thickness t_s for a different gate bias. The field has been probed at the middle of the InAs body thickness.

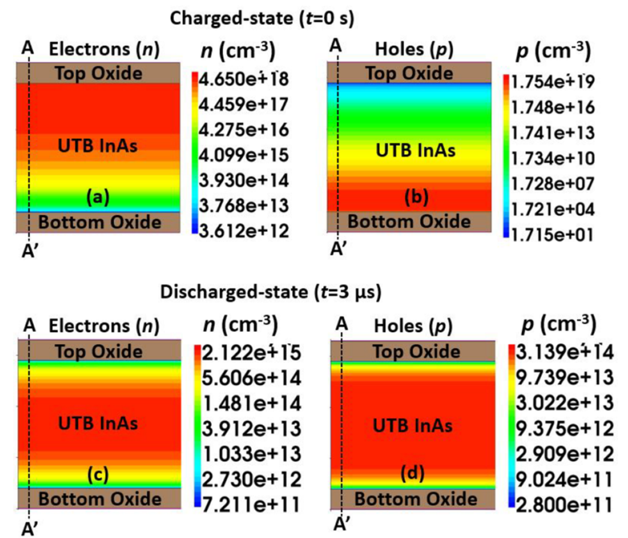

Fig. 5. Simulated 2-D cross section of induced charge carriers, (a), (b) at charged-state (t = 0 s), (c), (d) at discharged-state (t = 3 μs).

at the top (bottom) gate as shown in Fig. 5(a), (b). The situation where a high concentration (~10^{18} cm^{-3}) of both electrons and holes are simultaneously induced at opposite gate interfaces is hereafter referred to as charged-state. Since even at thermal equilibrium an EHB has been formed because of the gate-body workfunction difference, some opposite biasing (~$|\phi_{mT/B} - \phi_{midgap}|$) is required to make the body intrinsic. By applying a small (~0.25 V) negative (positive) bias at the top (bottom) gate, the body becomes intrinsic (~10^{15} cm^{-3}) as shown in the Fig. 5(c), (d). This situation is hereafter referred to as the discharged-state.

When the EHB is suddenly switched from its charged- to discharged-state, the charge carriers will decay via recombination processes (both radiative and non-radiative) to reach their final steady state value, see Fig. 6. The diffusion and recombination of holes can be observed from their transient density profiles in Fig. 6 where a spread in their vertical distribution along with a drop in their peak concentration are visible during the discharging-cycle, even when there is still an opposing electric field. However, electrons are mainly recombining and diffusion is less important, possibly because of a smaller slope (dn/dy) of their vertical distribution profile. Fig. 7 shows a radiative recombination rate, R_{rad}, (thus light emission) as high as ~10^{24} cm^{-3} s^{-1} at 0.5 μs after the on-set of discharging-cycle.

By continuously switching the gates, as shown in Fig. 8, the charge

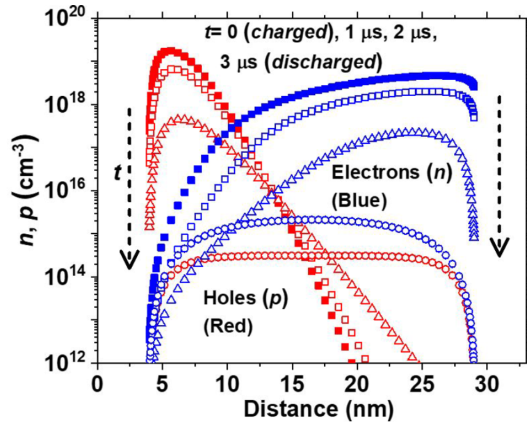

Fig. 6. Transient electron and hole density (along line AA′) at various time instances (t) during the discharging-cycle.

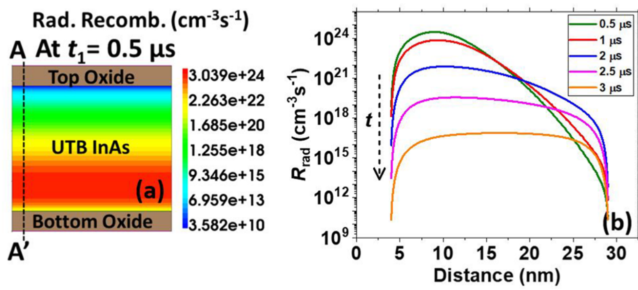

Fig. 7. (a) 2-D profile of radiative recombination rate at $t_1 = 0.5$ μs after the onset of the discharging-cycle. (b) Transient radiative recombination rate (along line AA′) at various time instances (t) during the discharging-cycle.

carriers are first thermally generated to form an EHB during the charging-cycle and later recombine during the discharging-cycle. In this way, steady light output via radiative recombination in the form of short (~0.5 μs) pulses can be maintained. The pulse width here is taken as the time in which the radiative recombination rate falls by about one order in magnitude. In these transient simulations, the voltage pulse was defined as a piecewise linear function with a rise/fall time ($t_{\text{rise/fall}} = 3$ μs), an on-time ($t_{\text{on}} = 5$ μs) and off time ($t_{\text{off}} = 1$ μs). The chosen t_{on} (5 μs) is sufficiently long for generating charge carriers from their intrinsic value to their high charged-state value.

Moreover, the EHB concentration at the charged-state and consequently R_{rad} can be further increased by applying a bias higher than 0.75 V, but that may degrade the dielectric layer over time. Note that the probed electric field in the HfO_2 layer at the charged-state ($|V_{\text{GT/B}}| = 0.75$ V) is ~6.5×10^5 V/cm which is well below its breakdown value [26]. However, the chosen biasing scheme is not the optimized one as it depends on the type of application. Other biasing schemes can also be explored, such as one involving the continuous switching of electron and hole channel positions between the top and bottom gate interfaces by applying higher positive/negative biases. This scheme will be more suitable for a device where both the top and bottom gate consist of the same metal with $\phi_{\text{mT}} = \phi_{\text{mB}} \sim \phi_{\text{midgap}}$.

Further, the role of thermal generation in our device can be analyzed from the current vs time ($I - t$) curve shown in Fig. 8(b). The switching current here is composed of two parts: the generation/recombination (GR) current and the displacement current. The displacement current is actually a result of the applied voltage switching in the capacitor and is equal to $C \cdot dV/dt$ where dV/dt is constant for the linear voltage ramp and C is the effective capacitance of the dual gate MOS stack which is also constant in the absence of any generation process. The GR current is the measure of carrier generation which in our case is thermal and is affected by parameters such as n_i, τ_{SRH} and B_{rad}. The integral of the GR current over time in the $I - t$ plot (indicated by the red horizontal lines) in Fig. 8(b) is equal to the total generated charge in that given time.

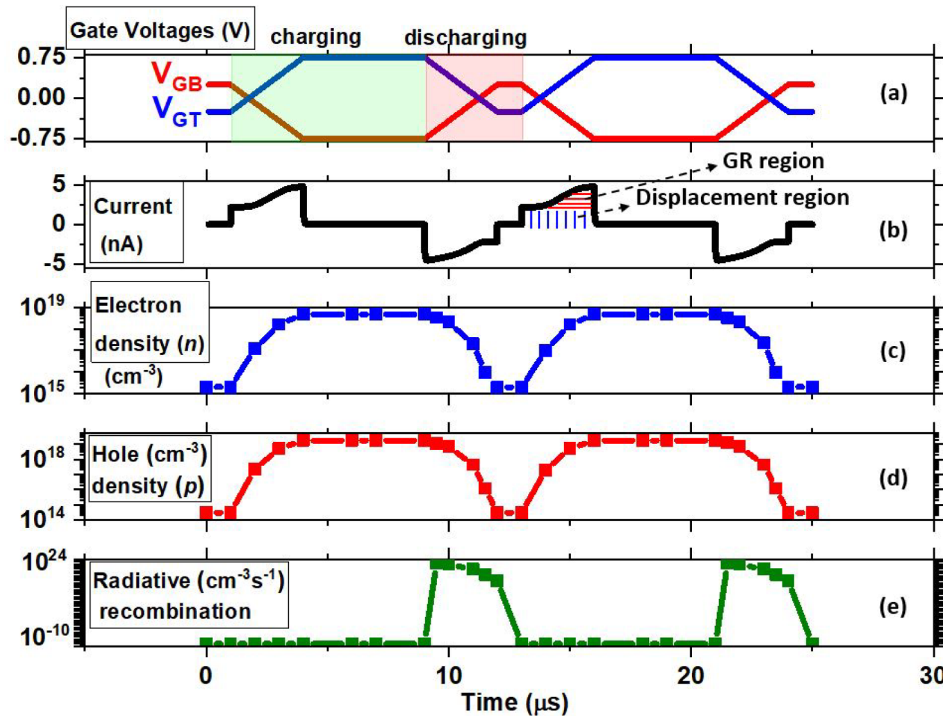

Fig. 8. Transient simulations of InAs EHB LED operation showing, (a) the gate voltage switching cycles, (b) the device current, (c) the peak electron density near the top gate interface, (d) the peak hole density near the bottom gate interface, (e) the maximum radiative recombination rate in the device. (charged-state $V_{\text{GT}} = 0.75$ V and $V_{\text{GB}} = -0.75$ V, discharged-state $V_{\text{GT}} = -0.25$ V and $V_{\text{GB}} = 0.25$ V, electrode area, $A_{\text{E}} = 7.85 \times 10^{-9}$ cm^2.).

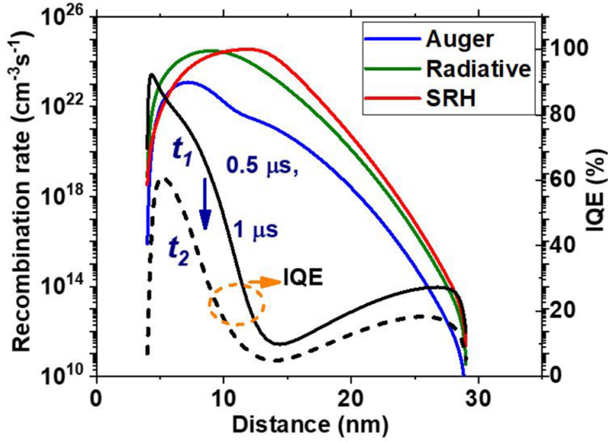

Fig. 9. Simulated recombination processes across AA′ at $t_1 = 0.5\ \mu$s after the on-set of discharging-cycle (left vertical-axis). The IQE profile across AA′ (right vertical-axis) at $t_1 = 0.5\ \mu$s and $t_2 = 1\ \mu$s.

In addition, we investigated the possible influence of a body side contact on the device operation when placed near the gated region for a ground reference, and compared that to the previous situation where no such side contact was used. While the device operation remains unaffected, the peak R_{rad} is however reduced (~by one order of magnitude) when a side metal contact with ϕ_{m}~ϕ_{midgap} was used. This reduction in R_{rad} is attributed to the carrier leakage via this side contact. The carrier leakage can be suppressed by using a side contact with either a high or low ϕ_{m} (in reference to ϕ_{midgap}). Moreover in practice, such contact can be placed further away from the gated region of the device which would further minimize the leakage.

3.3. Efficiency estimation

3.3.1. Internal quantum efficiency (IQE)

During the discharging-cycle, both radiative and non-radiative recombination processes such as Auger and SRH occur in the active region of the device. The left vertical-axis in Fig. 9 shows the contribution of SRH, radiative and Auger processes to the total recombination across the body thickness. We define the internal quantum efficiency (IQE) as the ratio of the radiative recombination rate (R_{rad}) to the total recombination rate [27]. The right vertical-axis in Fig. 9 shows the variation of IQE across the body thickness at different time instances during the discharging-cycle. As can be seen, a peak IQE as high as ~92% is obtained at $t_1 = 0.5\ \mu$s which gradually drops to ~60 % at $t_2 = 1\ \mu$s after the on-set of discharging-cycle. The integrated time-averaged IQE over one period across the whole device volume is ~29%. Note that both the peak radiative recombination rate and IQE are shifted towards the bottom gate. This is attributed to the asymmetric distribution of electrons and holes, and thus the $p{\cdot}n$ product (see Fig. 6) in the UTB, due to their unequal effective masses.

3.3.2. Power efficiency

From Fig. 8, we also estimated the power efficiency (η_{power}) of our device which is the ratio of optical power (energy) output to total electrical power (energy) input. The dynamic energy dissipation during the charging and discharging of a parallel plate capacitor can be expressed as [28]:

$$E_{\mathrm{elec}} = QV = V\int_0^T |I|dt, \tag{4}$$

where Q is the total charge generated in one cycle, V is the total voltage swing, I is the current and T is the cycle time. Similarly, the optical energy output during the switching cycle can be expressed as:

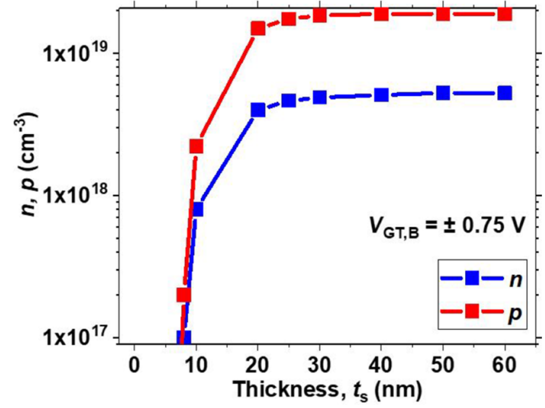

Fig. 10. Induced peak electron (n) and hole (p) concentrations at the charged-state condition at their respective gate interfaces for a varying InAs thickness t_{s}.

$$E_{\mathrm{opt}} = V\int_0^T I_{\mathrm{opt}}dt = qV\int_0^T R_{\mathrm{i-rad}}dt, \tag{5}$$

where $R_{\mathrm{i-rad}} = \iiint R_{\mathrm{rad}}dv$ is the integrated radiative recombination rate across the whole device volume.

Therefore,

$$\eta_{\mathrm{power}} = \frac{q\int_0^T R_{\mathrm{i-rad}}dt}{\int_0^T |I|dt} \times 100\%. \tag{6}$$

Using Eq. (6), we estimated the maximum η_{power} ~15% for our device. For this calculation we assumed the light extraction efficiency of our LED to be 100 % which in practice is difficult to achieve in such dual gate UTB structure. Measures such as the use of transparent electrodes or electrodes with regular openings should be considered for efficient light extraction.

3.4. Device optimization: body thickness

We also checked the effect of the InAs thickness t_{s} on the induced charge carrier concentrations and the radiative recombination rate. As shown in Fig. 10, the induced electron and hole densities initially increase with the thickness as described by Eqs. (1) and (2), valid for a fully depleted semiconductor body where the two opposite gate interfaces are electrostatically coupled. The electrostatic coupling gradually reduces for larger thicknesses, and as a result, the carrier concentration at their respective gate interfaces increases. For even larger body thicknesses, the charge carrier concentrations gradually saturate to the value which is mainly determined by the potential of their respective gate only.

For thicknesses below 10 nm, the sharp drop in carrier density is attributed to a very high electric field and resulting supercoupling effect [24]. Note that in our simulated dual gate structure, which features symmetric gate workfunctions and equal gate oxide thicknesses, the two gates are of equal strength and consequently the possibility of one gate winning over the other is rather small in the supercoupling regime. This however may not occur in e.g. SOI based devices where generally the top gate with a smaller gate oxide thickness controls the channel in that regime.

The radiative recombination rate on the other hand first increases with the thickness as the induced carrier concentrations increase and thereafter decreases as the spatial separation between the induced electron and hole layer increases as shown in Fig. 11. The maximum radiative recombination rate is at around $t_{\mathrm{s}} = 20$ nm which also justifies our initial choice for the thickness value used for the device simulations.

Moreover, as discussed, the supercoupling effect can be important in such dual gate UTB devices. Therefore, it is worthwhile to further

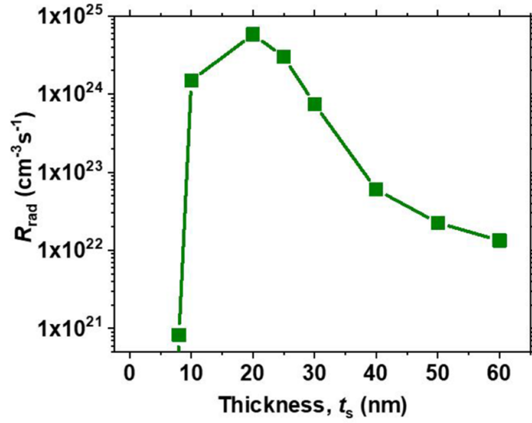

Fig. 11. Peak radiative recombination rate (R_{rad}) for a varying InAs thickness t_s where R_{rad} is noted at $t_1 = 0.5\,\mu s$ after the on-set of discharging-cycle.

estimate the critical thickness, t_s^* [24,25] below which such effect becomes important. The simplified expression for t_s^* as derived before in [24], assuming a strong inversion situation at the top gate ($V_{GT} > V_{TT}$), can be expressed as:

$$t_s^* = u_T \frac{\epsilon_s}{C_{oxB}(V_{FBB} - V_{GB})} \ln\left[\frac{N_a C_{oxT} C_{oxB}(V_{FBB} - V_{GB})}{q\,\epsilon_s\, n_i^2}\right] \tag{7}$$

where C_{oxB}, V_{GB} and V_{FBB} are the areal oxide capacitance, applied voltage and flatband voltage at the bottom gate respectively, C_{oxT}, V_{GT} and V_{TT} are the areal oxide capacitance, applied voltage and threshold voltage at the top gate respectively and N_a is the body doping density. To estimate t_s^* for our proposed device structure, we used Eq. (7), which is applicable to long channel devices as in this work but ignores quantum effects. For this estimation in case of our unintenionally doped device, we substituted N_a with the intrinsic carrier concentration (n_i~10^{15} cm^{-3}). At $V_{GB} = -0.75$ V, the calculated $t_s^* = 0.8$ nm, which is in fair agreement with our TCAD simulations (including quantum effects) where we start to see the supercoupling effect for t_s below 5 nm. Therefore, supercoupling is not much of a concern for our proposed dual gate structure with a symmetric top and bottom gate. It could however be an issue if a thicker bottom gate oxide is used. For example, the calculated t_s^* is about 26 nm for a 200 nm thick back oxide for the same V_{GB}.

As an application note, the proposed In(Ga)As based EHB LED can be monolithically integrated with an InAs photodiode, which could be attractive for a wide range of applications in the mid-infrared spectral region (2–10 μm) such as gas sensing and environmental monitoring [29,30].

3.5. Diode-mode operation

In addition to the proposed dual gate EHB device shown in Fig. 1, we investigated an alternative device structure, as shown in Fig. 12(a), where the InAs body is now directly sandwiched between two metal electrodes (with $\phi_{mT} = 4.9$ eV and $\phi_{mB} = 5.4$ eV) without any gate oxide in between. For these metal-semiconductor interfaces, a surface recombination velocity of $S_n = 2.5 \times 10^6$ cm/s and $S_p = 1.9 \times 10^6$ cm/s [19] were used in the simulations. All other simulation parameters were kept the same as summarized in Table 1.

The simulated energy band diagram for such a device at thermal equilibrium is shown in Fig. 12(b). Two Schotttky barriers have been formed with different barrier heights (ϕ_b) for electrons and holes at the opposite interfaces. Moreover, the workfunction induced electron and hole layers are also present at the top and bottom interface respectively. The charge transport in such a device can be considered to be equivalent to a series connection of an n-type and p-type Schottky diode with each having a different ϕ_b. The diode with a lower ϕ_b would then determine the current. The top interface determines the hole current while the bottom interface determines the electron current in the device, both via thermionic emission. The thermionic emission of charge carriers is also evident from the forward bias band diagram (see e.g. Fig. 12(c)) where both electron and hole quasi Fermi levels remain flat throughout the whole body [31]. The simulated $I - V$ characteristics of the device is shown in Fig. 12(d). Since $\phi_{bn} < \phi_{bp}$, the electron component will determine the total device current at low injection with an ideality factor, n, of unity. At high injection, where $n = 2$, the electron and hole current are comparable.

In such diode-mode operation, a lower steady-state IQE of ~16 % at $V_d = 0.5$ V was obtained which is expected to deteriorate further in the presence of tunneling processes, which were not accounted for. The observed lower IQE in the diode-mode operation is attributed to the enhanced SRH recombination rate in the presence of a more uniform distribution (p ~ n ~ constant) of charge carriers across the body thickness [32]. This is not the case for the switched-mode operation in the dual gate EHB device where the carrier concentrations gradually drop from their respective gate interfaces leading to $p \neq n$ and therefore a lower SRH rate (for the same SRH lifetime).

Furthermore, in practice, direct metal-semiconductor junctions are prone to the Fermi-level pinning effect [33] and therefore obtaining such Schottky barriers and resulting workfunction induced EHB is rather difficult. Particularly, in InAs, it has been reported that the Fermi level is normally pinned above the conduction band minimum [34]. In that respect, the proposed dual gate InAs EHB device based on the switched-mode operation is more practical as it is less prone to Fermi level pinning. Moreover it even shows higher IQE.

3.6. Si EHB LED

We also investigated the EHB LED concept for a wider bandgap material than InAs, such as Si, with a relatively low thermal generation rate. For such a material, the source of charge carriers in the form of highly doped p-type and n-type region on either sides of the intrinsic body, as also originally proposed for the EHB TFET [7], or side metal contacts with a high surface generation velocity should be adopted.

Fig. 13 shows the conceptual device architecture for the Si EHB LED with an additional doped region on either side. First, we will discuss the switched-mode operation of this gated Si EHB device. During its operation, both gate interfaces are switched between their charged- and discharged-state by applying the voltage pulses while keeping the side contacts to p$^+$ and n$^+$ regions grounded all the time, as shown in Fig. 13. The proposed device is capable of switching in the GHz frequency range, see Fig. 14 where the formation and recombination of EHB occurs in ns time period. The Si EHB emits low intensity (R_{rad}~2.5×10^{13} cm^{-3} s^{-1}) ns light pulses with an IQE of about ~10^{-3}%.

Next, we compare the performance of this Si EHB device with a conventional Si PIN diode of the same geometry as shown in Fig. 13 but without any provision of the top and bottom gate. The forward biased Si PIN diode shows a much higher light intensity compared to its EHB counterpart, with an IQE ~10^{-2}%. However, GHz switching in SOI PIN LEDs is challenging as discussed before in [35]. In this respect, the proposed Si EHB LED could be more attractive for an SOI based optocoupling application platform for its high speed switching capabilities.

Furthermore, the device efficiency of the Si EHB LED can be improved if the recombination at the p$^+$ and n$^+$ regions are effectively suppressed [4]. One way of achieving this is by physically separating the gated EHB regions from the heavily doped regions with an i-Si spacer region. However, the i-Si spacer region would then limit the device speed. So, again there is a trade-off between device speed and its efficiency [35]. Moreover, the carrier transit time through the intrinsic region also affects the device operation when it becomes comparable to the carrier lifetime for a longer diode length (L_i) and therefore the diode length also needs to be optimized for efficient device operation.

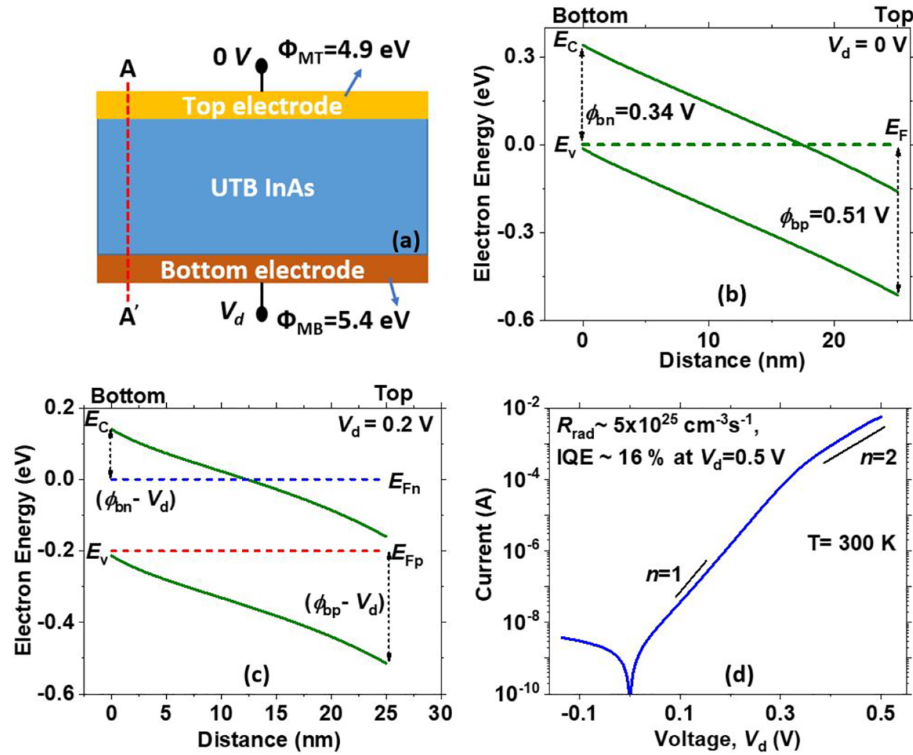

Fig. 12. InAs EHB device without gate oxides, (a) schematic cross-section, (b) simulated energy band diagram across AA′ at thermal equilibrium and (c) at forward bias, $V_d = 0.2$ V and (d) simulated *I-V* characteristics of the same device. Electrode area, $A_E = 7.85 \times 10^{-9}$ cm^2.

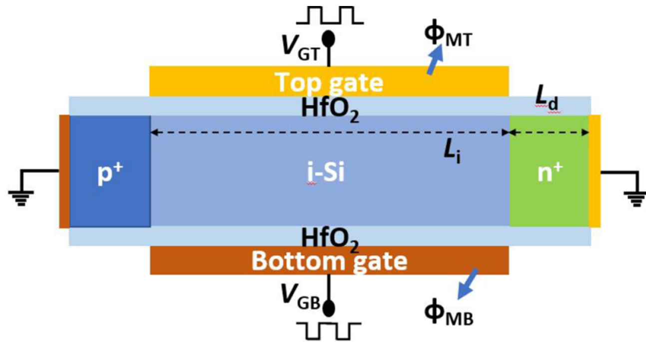

Fig. 13. Schematic cross section of the Si EHB LED with additional highly doped (~10^{20} cm^{-3}) regions on either side of the UTB intrinsic-Si body. Here, the silicon thickness $t_s = 12$ nm, $L_i = 0.5\,\mu$m, $L_d = 0.1\,\mu$m, $t_{oxT/B} = 4$ nm, $\phi_{MT} = 4.1$ eV and $\phi_{MB} = 5.1$ eV. For Si, SRH lifetimes, $\tau_n = 10^{-5}$ s and $\tau_p = 3 \times 10^{-6}$ s [19] and $B_{rad} = 10^{-14}$ cm^3 s^{-1} [36] were used.

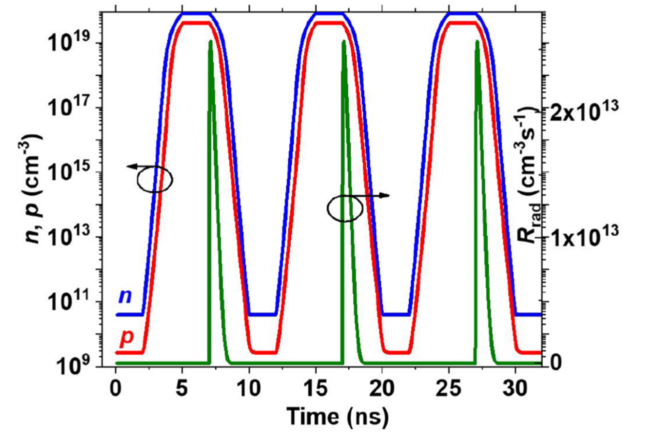

Fig. 14. Simulated switched-mode operation of the Si EHB LED in ns time scale showing the peak electron and hole density at the opposite gate interfaces (left vertical-axis) and the maximum radiative recombination rate in the device (right vertical-axis). (charged-state $V_{GT} = 1$ V and $V_{GB} = -1$ V, discharged-state $V_{GT} = -0.5$ V and $V_{GB} = 0.5$ V, $t_{on/off} = 2$ ns, $t_{rise/fall} = 3$ ns, gate electrode area, $A_E = 5 \times 10^{-9}$ cm^2.).

4. Conclusion

A novel switched-mode light emitting device based on the electrostatically induced EHB concept has been proposed. TCAD simulations show that the InAs based device is capable of switching in the µs range to emit light pulses of wavelengths corresponding to its effective bandgap. Monolithic integration of such an optical device along with (opto-) electronic devices in a UTB III-V on insulator (XOI) technology could be interesting for applications such as on-chip communication and sensing. The proposed device is more suitable for narrow bandgap materials since switching speed is limited by the bandgap through the thermal generation rate. In addition, the EHB LED concept is interesting for wider bandgap materials such as Si in a gated PIN configuration, where high speed switching in the GHz range is possible, which could be explored for SOI based optocoupling applications.

Acknowledgment

The authors acknowledge the partial financial support from the NWO Domain Applied and Engineering Sciences (TTW), The Netherlands (OTP 2014, under Project 13145). The authors would also like to thank J. Schmitz, L.K. Nanver and S. Dutta for fruitful discussions and critically reading this manuscript.

Appendix A

In the absence of impact ionization and under dark conditions, the carrier generation will be mainly via thermal processes. The thermal generation rate can be distinguished by four processes: bulk space-charge (scr) generation (G_1), band-to-band generation (G_2), quasi-neutral bulk generation (G_3) and surface generation (G_4). G_1 is characterized by the generation time (τ_g) [37] and G_2 is characterized by the radiative recombination coefficient (B_{rad}) which is equally important for direct bandgap semiconductors. For the UTB based EHB concept G_3 can be ignored. Further, we also assume ideal interfaces hence surface generation (G_4) is not present.

For convenience sake, we focus on a 1-D system with uniform concentrations. Using the continuity equation for electrons (ignoring holes) we can write [37]:

$$\frac{dn}{dt} = G = G_1 + G_2 \tag{8}$$

where G is the net generation rate due to various mechanisms.

For bulk scr generation when $pn<n_i^2$, which is actually the inverse of SRH recombination, the generation rate can be expressed as [37]:

$$G_1 = -R_{\mathrm{SRH}} = \frac{n_i^2}{\tau_p n_1 + \tau_n p_1} = \frac{n_i}{\tau_g} \tag{9}$$

Assuming SRH lifetimes $\tau_n = \tau_p = \tau_{\mathrm{SRH}}$ and defect level (E_T) coinciding with the intrinsic Fermi level (E_{FI}), Eq. (9) can be re-written as:

$$G_1 = \frac{n_i}{2\tau_{\mathrm{SRH}}} \tag{10}$$

The band-to-band generation can be expressed as:

$$G_2 = \frac{n}{\tau_{\mathrm{rad}}} = B_{\mathrm{rad}} n_i^2, \tag{11}$$

So, substituting Eqs. (10) and (11) in Eq. (8), we can write:

$$\frac{dn}{dt} = \frac{n_i}{2\tau_{\mathrm{SRH}}} + B_{\mathrm{rad}} n_i^2. \tag{12}$$

Now, the number of electrons, n_0, generated in the total time t_{th} can be determined as:

$$n_0 = \int_0^{t_{th}} G dt = \int_0^{t_{th}} \left(\frac{n_i}{2\tau_{\mathrm{SRH}}} + B_{\mathrm{rad}} n_i^2\right) dt. \tag{13}$$

In principle the generation components do not have a strong time dependence, and consequently:

$$t_{th} = \frac{n_0}{\left(\frac{n_i}{2\tau_{\mathrm{SRH}}} + B_{\mathrm{rad}} n_i^2\right)}. \tag{14}$$

From the above simplified expression, it can be concluded that the generation time t_{th} rises exponentially with the bandgap through n_i and therefore narrow (and direct) bandgap materials are more effective for the thermally generated EHB concept.

References

[1] Roelkens G, Liu L, Liang D, Jones R, Fang A, Koch B, Bowers J. III-V/silicon photonics for on-chip and intra-chip optical interconnects. Laser Photon Rev 2010;4(6):751–79.
[2] Thomson D, Zilkie A, Bowers JE, Komljenovic T, Reed GT, Vivien L, Marris-Morini D, Cassan E, Virot L, Fédéli J-M, et al. Roadmap on silicon photonics. J Opt 2016;18(7):073003.
[3] Roelkens G, Abassi A, Cardile P, Dave U, De Groote A, De Koninck Y, Dhoore S, Fu X, Gassenq A, Hattasan N, et al. III-V-on-silicon photonic devices for optical communication and sensing in photonics vol. 2. Multidisciplinary Digital Publishing Institute; 2015. p. 969–1004.
[4] Hoang T, LeMinh P, Holleman J, Schmitz J. Strong efficiency improvement of SOI-LEDs through carrier confinement. IEEE Electron Device Lett 2007;28(5):383–5.
[5] Jones EC, Ishida E. Shallow junction doping technologies for ULSI. Mater Sci Eng R Rep 1998;24:1–80.
[6] Gupta G, Rajasekharan B, Hueting RJE. Electrostatic doping in semiconductor devices. IEEE Trans Electron Dev Aug 2017;64:3044–55.
[7] Lattanzio L, Michielis LD, Ionescu AM. The electron-hole bilayer tunnel FET. Solid-State Electron 2012;74:85–90.
[8] Zhu Z, Zhu H, Xu M, Zhong J, Zhao C, Chen D, Ye T. A novel fin electron-hole bilayer tunnel field-effect transistor. IEEE Trans Nanotechnol Nov 2014;13:1133–7.
[9] Padilla J, Medina-Bailon C, Alper C, Gamiz F, Ionescu A. Confinement-induced InAs/GaSb heterojunction electron–hole bilayer tunneling field-effect transistor. Appl Phys Lett 2018;112(18):182101.
[10] Rodriguez N, Gamiz F, Cristoloveanu S. A-RAM memory cell: concept and operation. IEEE Electron Device Lett 2010;31(9):972–4.
[11] Gupta G, Mema F, Hueting RJE. InAs electron-hole bilayer LED. 2019 Joint International EUROSOI Workshop and International Conference on Ultimate Integration on Silicon (EUROSOI-ULIS). IEEE; 2019.
[12] Lim H-K, Fossum JG. Threshold voltage of thin-film silicon-on-insulator (SOI) MOSFET's. IEEE Trans Electron Devices 1983;30:1244–51.
[13] Alper C, Lattanzio L, Michielis LD, Palestri P, Selmi L, Ionescu AM. Quantum mechanical study of the germanium electron-hole bilayer tunnel FET. IEEE Trans Electron Devices 2013;60:2754–60.
[14] Krishnamurthy S, Berding M. Full-band-structure calculation of Shockley-Read-Hall recombination rates in InAs. J Appl Phys 2001;90(2):848–51.
[15] Li N, Harmon ES, Hyland J, Salzman DB, Ma T, Xuan Y, Ye P. Properties of InAs metal-oxide-semiconductor structures with atomic-layer-deposited Al2O3 Dielectric. Appl Phys Lett 2008;92(14):143507.
[16] Wu Y-C, Chang EY, Lin Y-C, Kei C-C, Hudait MK, Radosavljevic M, et al. Study of the inversion behaviors of Al2O3/InxGa1-xAs metal-oxide-semiconductor capacitors with different In contents. Solid-State Electron 2010;54(1):37–41.
[17] Ko H, Takei K, Kapadia R, Chuang S, Fang H, Leu PW, et al. Ultrathin compound semiconductor on insulator layers for high-performance nanoscale transistors. Nature 2010;468(7321):286.
[18] Takei K, Chuang S, Fang H, Kapadia R, Liu C-H, Nah J, et al. Benchmarking the performance of ultrathin body InAs-on-insulator transistors as a function of body thickness. Appl Phys Lett 2011;99(10):103507.
[19] Synopsys Inc. Mountain View, CA, USA, Sentaurus TCAD, version l-2016.03 ed.; 2016.
[20] Arora ND, Hauser JR, Roulston DJ. Electron and hole mobilities in silicon as a function of concentration and temperature. IEEE Trans Electron Devices 1982;29(2):292–5.
[21] Canali C, Majni G, Minder R, Ottaviani G. Electron and hole drift velocity measurements in silicon and their empirical relation to electric field and temperature. IEEE Trans Electron Devices 1975;22(11):1045–7.
[22] Ancona M, Tiersten H. Macroscopic physics of the silicon inversion layer. Phys Rev B 1987;35(15):7959.
[23] Ancona M, Iafrate G. Quantum correction to the equation of state of an electron gas in a semiconductor. Phys Rev B 1989;39(13):9536.
[24] Eminente S, Cristoloveanu S, Clerc R, Ohata A, Ghibaudo G. Ultra-thin fully-depleted SOI MOSFETs: special charge properties and coupling effects. Solid-State

Electron 2007;51(2):239–44.
[25] Navarro C, Bawedin M, Andrieu F, Sagnes B, Martinez F, Cristoloveanu S. Supercoupling effect in short-channel ultrathin fully depleted silicon-on-insulator transistors. J Appl Phys 2015;118(18):184504.
[26] Wheeler D, Seabaugh A, Froberg L, Thelander C, Wernersson L-E. Electrical properties of HfO2/InAs MOS capacitors. Proc. semiconductor device research symposium. IEEE; 2007. p. 1–2.
[27] Karpov S. ABC-model for interpretation of internal quantum efficiency and its droop in III-nitride LEDs: a review. Opt Quantum Electron 2015;47(6):1293–303.
[28] Rabaey JM, Chandrakasan AP, Nikolic B. Digital integrated circuits vol. 2. Prentice hall Englewood Cliffs; 2002.
[29] Matveev B, Aidaraliev M, Gavrilov G, Zotova N, Karandashov S, Sotnikova G, Stus N, Talalakin G, Il'inskaya N, Aleksandrov S. Room temperature InAs photodiode–InGaAs LED pairs for methane detection in the mid-IR. Sens Actuators B: Chem 1998;51(1–3):233–7.
[30] Krier A. Mid-infrared semiconductor optoelectronics vol. 118. Springer; 2007.
[31] Sze SM, Ng KK. Physics of semiconductor devices. John Wiley & Sons 2006.
[32] Puliyankot V, Hueting RJE. One-dimensional physical model to predict the internal quantum efficiency of Si-based LEDs. IEEE Trans Electron Devices Jan. 2012;59:26–34.
[33] Tung RT. Chemical bonding and Fermi level pinning at metal-semiconductor interfaces. Phys Rev Lett 2000;84(26):6078.
[34] Olsson L, Andersson C, Håkansson M, Kanski J, Ilver L, Karlsson UO. Charge accumulation at InAs surfaces. Phys Rev Lett 1996;76(19):3626.
[35] Puliyankot V, Piccolo G, Hueting RJE, Schmitz J. Toward GHz switching in SOI light emitting diodes. IEEE Trans Electron Devices 2018;99:1–8.
[36] Gerlach W, Schlangenotto H, Maeder H. On the radiative recombination rate in silicon. Physica Status Solidi (a) 1972;13(1):277–83.
[37] Schroder DK. Semiconductor material and device characterization. John Wiley & Sons; 2006.